



Science Arts & Métiers (SAM)

is an open access repository that collects the work of Arts et Métiers Institute of Technology researchers and makes it freely available over the web where possible.

This is an author-deposited version published in: <https://sam.ensam.eu>
Handle ID: <http://hdl.handle.net/10985/24182>

To cite this version :

Anton SMIRNOV, Svetlana TEREKHINA, Tatiana TARASOVA, Lamine HATTALI, Sergey GRIGORIEV - From the development of low-cost filament to 3D printing ceramic parts obtained by fused filament fabrication - The International Journal of Advanced Manufacturing Technology - Vol. 128, n°1-2, p.511-529 - 2023

Any correspondence concerning this service should be sent to the repository

Administrator : scienceouverte@ensam.eu



From the development of low-cost filament to 3D printing ceramic parts obtained by fused filament fabrication

Anton Smirnov¹ · Svetlana Terekhina² · Tatiana Tarasova¹ · Lamine Hattali³  · Sergey Grigoriev¹

Abstract

The cost of manufacturing a structural ceramic component is a direct function of production quantity. Small-quantity production, such as prototypes manufactured by conventional methods, leads to long production times and high unit costs. The advent of fused filament fabrication of ceramic (FFFC) technology has created an opportunity to reduce lead time and cost and produce complex-shaped bodies with tailored sized and controlled porosity in small-quantity production runs, which is an advantage over traditional methods of fabrication of ceramic products. In this work, we propose to study the feasibility of manufacturing a low-cost composite filament, for FFFC processing, based on micrometric alumina (Al_2O_3) powder and polylactic acid (PLA) polymer as a binder system without any additive. Three compositions with the ceramic-to-polymer ratios (by volume) were considered: 70% Al_2O_3 /30% PLA, 60% Al_2O_3 /40% PLA, and 50% Al_2O_3 /50% PLA. For that, the customized technological chain is adapted. It consists of four principal steps: (i) grinding in a ball mill and drying the raw powders; (ii) extrusion into ceramic-polymer filament; (iii) printing of ceramic-polymer samples; and (iv) thermal debinding and sintering samples to obtain the ceramic product. The physical, microstructural, and mechanical properties of raw materials, composite filament, and green and sintering samples are investigated and the optimal composition is chosen dependent on both homogeneous repartition of the Al_2O_3 powder and the printability of filament. The 3D sintered material obtained by 60% Al_2O_3 /40% PLA composite filament shows the best flexural strength value of 332 ± 21 MPa with a relative density of $\sim 91\%$, which may be sufficient for several technical applications. Note that the 60% Al_2O_3 /40% PLA filament composite can easily be used to print a complex geometry using a standard nozzle of 0.4 up to 0.8 and does not show signs of brittleness during the printing process allowing it to become a promising material for the FFFC process. Based on the results of this paper and previous studies, FFFC technology can be a technically feasible and economically viable process for manufacturing ceramic components under certain conditions.

Keywords Additive manufacturing · Fused filament fabrication · Ceramic-polymer composite · Alumina · PLA

✉ Lamine Hattali
lamine.hattali@universite-paris-saclay.fr

Anton Smirnov
a.smirnov@stankin.ru

Svetlana Terekhina
svetlana.terekhina@ensam.eu

Tatiana Tarasova
t.tarasova@stankin.ru

Sergey Grigoriev
s.grigoriev@stankin.ru

¹ Moscow State University of Technology “STANKIN”, 3-A Vadkovskiy Pereulok, 127055 Moscow, Russia

² Arts et Métiers, Campus Angers - Laboratory LAMPA, 2 Bd du Ronceray, 49035 Angers Cedex 1, France

³ Université Paris-Saclay, CNRS, FAST, 91405 Orsay, France

1 Introduction

Ceramics have been used in a wide range of modern industrial applications, such as aerospace, defense, electronics, automotive, chemical, and biomedical engineering [1–4]. The properties that make them versatile materials include high mechanical strength and hardness, low thermal conductivity, high wear, good corrosion resistance, and viable optical, electrical, and magnetic performance. Generally, the traditional ceramic forming processes—such as injection molding, powder pressing centrifugal casting, strip casting, and uniaxial and isostatic pressing, to name just a few—have many uses in ceramic production, but they are subjected to some limitations, imposed by the nature of the process itself. On the one hand, production of highly

complex shapes with, e.g., interconnected holes or lattice-like geometry represents a challenge that becomes complicated if not impossible or expensive to produce using conventional ceramic processes. On the other hand, the machining of ceramic components tends to be extremely difficult owing to their extreme hardness and brittleness. Manufacturing each workpiece requires high costs and investments. For example, the use of diamond cutting, grinding tools, and achievement of high surface quality and dimensional accuracy are estimated to represent more than 70–80% of the total manufacturing costs [5–7]. Today, the demand for complex geometries with diverse customization options and favorable production methods is continuously increasing. For this reason, the need to manufacture ceramic products with complex shapes that require minimal additional machining is extremely important and promising. The introduction and emergence of three-dimensional (3D) printing technologies, also referred to as additive manufacturing (AM), into the manufacturing of ceramic components opens completely new possibilities for solving the challenges and limitations mentioned above. During the last few years, more precisely between 2008 and 2018, more than 1110 patents on ceramics were published, with the majority focusing on the development of material formulations for AM technologies, followed by patents on process innovations [8–10]. The great development of several main methods for obtaining ceramic materials with complex shapes has been established. Among the different available AM techniques such as ceramic stereolithography (CSL) [11], selective laser sintering (SLS) [12–14], selective laser melting [15], ceramic paste extrusion (CPE) [16, 17], to mention just a few, fused filament fabrication (FFF), sometimes denoted fused deposition modeling (FDM™) or specifically for manufacturing ceramics, fused filament fabrication of ceramics (FFFC) [18, 19], is the trendiest technique and represents a relatively novel approach to ceramic production. Although the CSL and SLS process approaches have their advantages, e.g., high forming precision, the drawbacks are related to difficulty in use, post-processing requirements, and environmental aspects, as well as the investment cost for a single device. Nowadays, several of these issues are resolved using the FFF process. The latter is cheap, accessible, highly flexible, and uses stable and easily transportable precursor materials. The FFF process consists of heating a thermoplastic filament slightly above its melting point inside a nozzle. The viscous material is then extruded out of a die, and deposited sequentially and additively, according to the programmed path (x, y, and z-axis) corresponding to the G-code file [20, 21].

In the past and nowadays, there were many attempts to improve or modify the thermoplastic filament properties

by adding small amounts of diverse powders (carbon, wood, metallic, ceramic, etc.) or fiber materials [22–24]. By filling thermoplastics, considered the binder, with ceramic powder in very high solid contents (> 45 vol %), it is possible to print objects that can be debinded and sintered to attain densities comparable to those fabricated via conventional approaches [25–30]. Most of the polymers used in the FFF process can also be used as binder for ceramic manufacturing. However, binders and ceramic powders need good compatibility to ensure homogeneity in mixing and to avoid phase separation during processing. Various characteristics of the ceramic feedstock affect the printing such as the size of ceramic particles, their distribution in the filament, and suitable rheology for the applied process to ensure shape retention and good bonding of the filament. Note that the appropriate flexibility and strength of the resulting filament should be sufficient to spool the filament for its storage and ensure both de-pool and avoid buckling during printing. The viscosity of the thermoplastic binder should be low enough to enable the flow through the printing nozzle with minimum resistance to reduce the backup pressure [28]. For highly filled polymeric compounds, this is quite challenging to achieve, especially for submicron powders, due to the high tendency for particle agglomeration, which increases the resistance to flow [31]. In addition, it is necessary to ensure appropriate adhesion to the building platform to not damage the part during the extraction from it, and good bonding between the deposited layers to achieve their good mechanical properties [32]. Furthermore, the thermoplastic binder should be easily removable without defects [33]. In this regard, it should be noted that defects play a very important role during the printing of products since they reduce the mechanical properties of finished products. The presence of voids leads to a decrease in the density of the samples. All these requirements form a technical obstacle and therefore hinder the expansion of the FFFC process for the production of ceramic components. However, several studies have tried to meet the maximum of the above requirements as much as possible by adding other components to binders such as elastomers, tackifiers, waxes, or plasticizers [34–37]. Aluminum oxide (Al_2O_3), silicon nitride (Si_3N_4), and yttria-stabilized zirconia (YSZ) have all been used to fabricate 3D parts using the FFF process [28, 35, 37–40]. To obtain a final dense ceramic, it is necessary to remove the binder or its multi-component system during the debinding process (chemical and/or thermal). A sintering step is required for the densification of ceramic particles and gives the part its final material properties and microstructures. Recently, commercial filaments emerged for FFF ceramic including, alumina and silicon carbide-based systems (SiC) from Nanoe [41] and zirconium silicate filament from the Virtual Foundry [42]. However, for

the latter, no information about the binder material recipes employed is publicly available, and details of the size of ceramic particles are missing. All commercially available filaments have common characteristics—the recommended nozzle diameter is always at least 0.6 mm and the filaments are brittle. For Virtual Foundry, they recommend pre-heating the feedstock before its entry point into the feeder to prevent its breakage, whereas the ceramic composite filaments from Nanoe are usable only with a specific printer equipped with a direct-drive filament system (Raise 3D, Prusa, flashForge...).

The present paper is focused on the feasibility study of a low-cost $\text{Al}_2\text{O}_3/\text{PLA}$ composite filament usable in an open source FFF 3D printer. Three compositions with the following ceramic-to-polymer ratios (by volume) 70% $\text{Al}_2\text{O}_3/30\%$ PLA, 60% $\text{Al}_2\text{O}_3/40\%$ PLA, and 50% $\text{Al}_2\text{O}_3/50\%$ PLA were studied. The composition composite filament is comprised of environmentally friendly and biodegradable PLA as the thermoplastic binder and Al_2O_3 ceramic powders. The novelty lies in the use of a binder system with only one polymeric material, which means no additives, such as waxes, dispersant agents, stabilizers, or tackifiers were added. Although some ceramic composite filaments for the commercial FFF process exist to date, they remain expensive, and their manufacturers recommend several modifications or specific printers. The $\text{Al}_2\text{O}_3/\text{PLA}$ composite filament developed within this study, to the best knowledge of the authors, does not have the abovementioned limitations, except for using a direct drive system in a 3D printer. Note that the filament can be easily printed using a standard nozzle of 0.4 up to 0.8 mm and does not show signs of brittleness during the printing process. In addition, whatever the part shape, no additional adhesives such as glue and tape were used to fix a part on the printing bed, as is often the case with composite filaments [42].

2 Materials and methods

2.1 Materials and filament composition choice

Commercially available powders of alumina Al_2O_3 ($d_{50} \sim 40 \mu\text{m}$, Plasmotherm Ltd., Moscow, Russia) and the thermoplastic polylactic acid PLA ($d_{50} \sim 35 \mu\text{m}$, eSun Ltd., Shenzhen China) were chosen as a feedstocks. Alumina was chosen as a ceramic component, because it has high strength characteristics and chemical resistance. It is used in various branches of engineering for the manufacture of final products with high strength characteristics and chemical resistance, whereas the polymer binder polylactide (PLA) is chosen for its low cure shrinkage, wide use in the FFF process, and relatively low cost. In addition, it is

a biodegradable polymer, which is an advantage from the standpoint of ecology. Its monomer, lactic acid, is made from renewable resources such as corn and sugar cane. In our study, the $\text{Al}_2\text{O}_3/\text{PLA}$ mixture consists of 50 up to 70 vol. % of Al_2O_3 . The choice of these compositions is based on our preliminary experimental work and the literature review [28–30]. The latter suggests that if the ceramic powder content is lower than 45 vol%, it is very difficult, or if not impossible, to obtain a filament with an appropriate flexibility and strength that enables it to both spool and de-spool for its storage and printing and avoid buckling during printing. Also, the viscosity of the thermoplastic binder should be low enough to minimize the flow resistance through the printing nozzle and reduce the backup pressure. For highly ceramic powdered content, this is quite challenging to achieve.

2.2 Preparation and fabrication of ceramic-polymer composites filaments

The colloidal method was chosen to obtain a ceramic-polymer mixture with a homogenous particle distribution. The

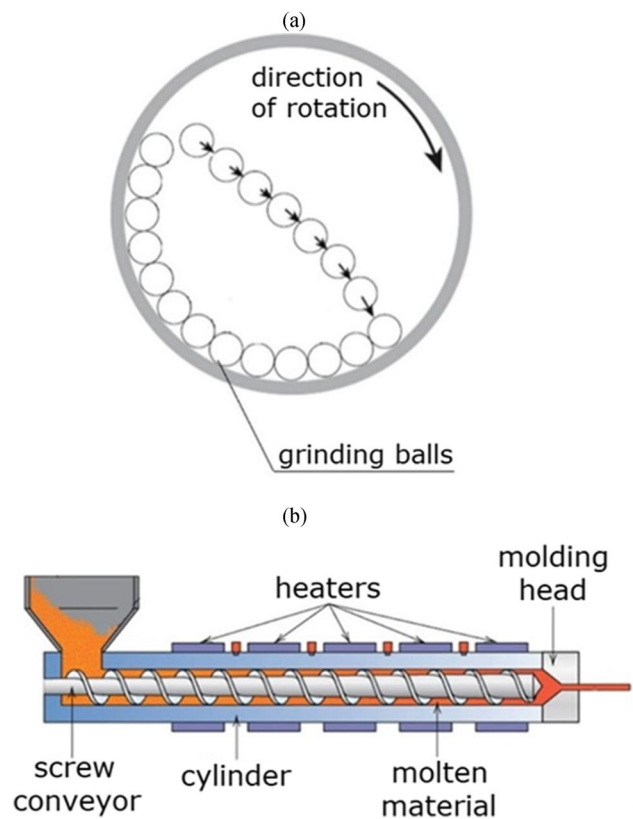


Fig. 1 Preparation and fabrication of ceramic-polymer filament, **a** the principle of the ball mill, **b** the working scheme of the single screw extruder

latter is associated with the fact that it allows obtaining large volumes of material with minimal time and energy costs. It also permits the ensuring uniform distribution of all composition components and helps to avoid particle agglomeration during stirring [43–45]. The mixtures were ball-milled in an ML-1C (Promstroimash, Kaluga, Russia) for 24 h (Fig. 1a and b). Alumina balls ($\phi = 2$ mm) and distilled water were used, respectively, as grinding and liquid media. The ball-to-powder weight ratio was 5:1, with a milling speed of 125 rpm.

The obtained suspension was dried in a vacuum desiccator VO 400 (Memmert, Germany) for 24 h at 90 °C and then sieved on a vibratory sieve shaker AS 200 Basic (Retsch, Haan, Germany). The prepared mixture was passed into pellets on a machine for hot pressing samples, OPAL 480 (ATM, Mammelzen, Germany), for 45 min at a pressure of 175 bars and a temperature of 185 °C. The pellets were then loaded into the hopper of a Wellzoom desktop extruder (Wellzoom, Shanghai, China), and a continuous filament of 1.7 ± 0.1 mm diameter was produced for 3D printing at 220 °C. The diameter was measured using a digital caliper, and the ovality of the filament was checked by optical microscopy. All obtained filaments were stored in a desiccator cabinet to prevent water absorption from the environment.

2.3 Additive manufacturing of samples

The feasibility of FFFC printing using $\text{Al}_2\text{O}_3/\text{PLA}$ filament is tested using a commercial Black Widow 3D printer (Tevo 3D, Zhanjiang, China) coupled with a PC using the Repetier-Host software in version 2.2.4 and the slicer software Simplify3D in version 4.1.2. Three stages were needed to perform the printing. The first is to choose the best $\text{Al}_2\text{O}_3/\text{PLA}$ composition, which permits to print the filament easily with minimum defects and ensures its flexibility and strength to spool and de-spool it for printing. Then, the printing parameters of the appropriate $\text{Al}_2\text{O}_3/\text{PLA}$ composition were optimized based on the obtained results and performed tests. For example, the z-axis adjustment plays an important role in obtaining a dense and smooth first layer of the sample. The range of extrusion temperature (from 190 to 250 °C) and printing speed (from 1.25 to 2 mm/min) were chosen based on further study [46, 47]. At the lowest considered temperature ($T = 190$ °C), the composite filament was not melted sufficiently and was forced through the nozzle, whereas at the highest one ($T = 250$ °C), the samples warped due to low viscosity. Finally, once the FFFC parameters were established, three-dimensional samples of cylindrical shape (25 mm diameter and 2 mm height) and geometries with complex shapes were manufactured.

2.4 Filaments and samples characterizations

Dispersion and granulometric composition of powders An Occhio 500 nano image analyzer (Occhio SA, Belgium) according to ISO 13322–1:2014 was used to obtain information about the statistical dispersion of powder. Chemical analysis and the morphology of particles were determined using a Vega 3 LMH scanning electron microscope (Tescan, Czech Republic).

X-ray analysis An empyrean X-ray diffractometer (PANalytical, Almelo, Netherlands) was used to determine the phase composition of the initial ceramic powder (Cu-K α spectrum, wavelength 1.5405981 Å, voltage 60 kV, beam current 30 mA) with a shooting range angle of 2θ from 20 to 70° and a shooting step of 0.05°. Qualitative analysis of crystal phases was carried out using the ICDD PDF-4 electronic database, ICDD-PDF card number 00–046–1212. To confirm the polymer structure, the method of infrared spectroscopy (IR) with Fourier transform on the Vertex 70 IR spectrometer (Bruker, USA) was used.

Density A helium pycnometer model AccuPyc 1340 (Micromeritics, USA) was used to measure the density of ceramic-polymer compounds. The powder compound was dried in a drying cabinet for 2 h at a temperature of 80 °C and then cooled in a desiccator to room temperature. The dried sample was weighed on the analytical balance AND GR-300 (Japan), with an accuracy of 0.0001 g, and placed in a helium pycnometer.

After measuring the true density of the compounds, the theoretical density was calculated using Eq. (1):

$$\rho_{theor} = \frac{c_a \rho_a + c_b \rho_b + \dots}{100} \quad (1)$$

where ρ_a and ρ_b are the densities of the corresponding components a and b, and c_a and c_b are the percentage volume of the corresponding components.

Optical microscopy and SEM analysis The microstructure and micro-relief of the sample surfaces were studied using an Axio Observer D1m optical microscope (Carl Zeiss, Germany) and a scanning electron microscope Phenom G2 PRO (Thermo Scientific Phenom, Netherlands) with a built-in energy dispersion EDX analyzer. The study of the filament surface was carried out using a stereomicroscope RZ (Meiji Techno, Japan).

Rheological properties To evaluate the possibility of obtaining extruded filament for 3D printing, rheology tests were performed on a rotational rheometer Mars (Thermo

Fisher Scientific Inc., USA) with a “plane-plane” working unit geometry (diameter 20 mm, 1 mm offset). Oscillatory measurements were used to increase the range of shear rate, which can occur when measurements are performed in constant rotational mode. Testing conditions were the following: (i) frequency dependence of the dynamic modulus components at a deformation amplitude of 1% (the deformation frequency was varied from 0.1 to 100 Hz); (ii) creep tests at a constant load of 10, 100, and 500 Pa for an unfilled PLA with subsequent removal of the load (recovery stage); and (iii) dependence of viscosity on shear rate (the shear rate range was increased stepwise from 0.001 to 10 s⁻¹ by holding at each stage for 30 s). According to the recommended temperature range for the materials, the measurements were taken in the range of 200–220 °C for the PLA and 200–240 °C for the Al₂O₃/PLA filament.

Mechanical characterization The Al₂O₃/PLA filament is characterized using the tensile test. The geometry of tensile samples was fabricated for the Type I specimen of the ISO 527–1:2019 standards [48]. An initial gauge length of 50 mm was set for all the measurements. The test was performed at a speed of 1 mm/min until the specimens broke. The obtained results were compared with the values of reference samples printed from PLA filament. To evaluate the flexural strength of specimens, a biaxial flexure test (DIN EN ISO 6872:2019) was used [49]. A sintered disc-shaped specimen with a diameter and thickness of 21 mm and 1.6 mm was placed onto a device with three balls of 3 mm in diameter made of hardened steel and disposed on a holder (10 mm in diameter) at 120° to each other. The load was applied using a plain head of 1.6 mm in diameter at a crosshead speed of 1 mm/min. According to Kirstein and Woolley [50], the maximum tensile stress in the center of the disc face is approximately independent of the number of support points and can be described by:

$$\sigma_{max} = -\frac{3}{4\pi} P \frac{X - Y}{b^2} \quad (2)$$

$$X = (1 + \nu) \ln \left(\frac{r_2}{r_3} \right)^2 + \frac{(1 - \nu)}{2} \left(\frac{r_2}{r_3} \right)^2 \quad (3)$$

$$Y = (1 + \nu) \left[1 + \ln \left(\frac{r_1}{r_3} \right)^2 \right] + (1 - \nu) \left(\frac{r_1}{r_3} \right)^2 \quad (4)$$

where P is the maximum force measured during the test, b is the thickness of the specimens at the origin of fracture, r_1 is the radius of the circle defined by the three balls, r_2 is the radius of the loaded area, r_3 is the radius of the

specimen, and ν is the Poisson’s ratio of the tested material. All mechanical tests were realized using the Instron Electropuls E10000 (Instron, USA) at standardized conditions (~21 °C and ~55% relative humidity). At least twelve repetitions were performed for each test.

3 Results and discussion

3.1 Phase analysis, morphology, and density

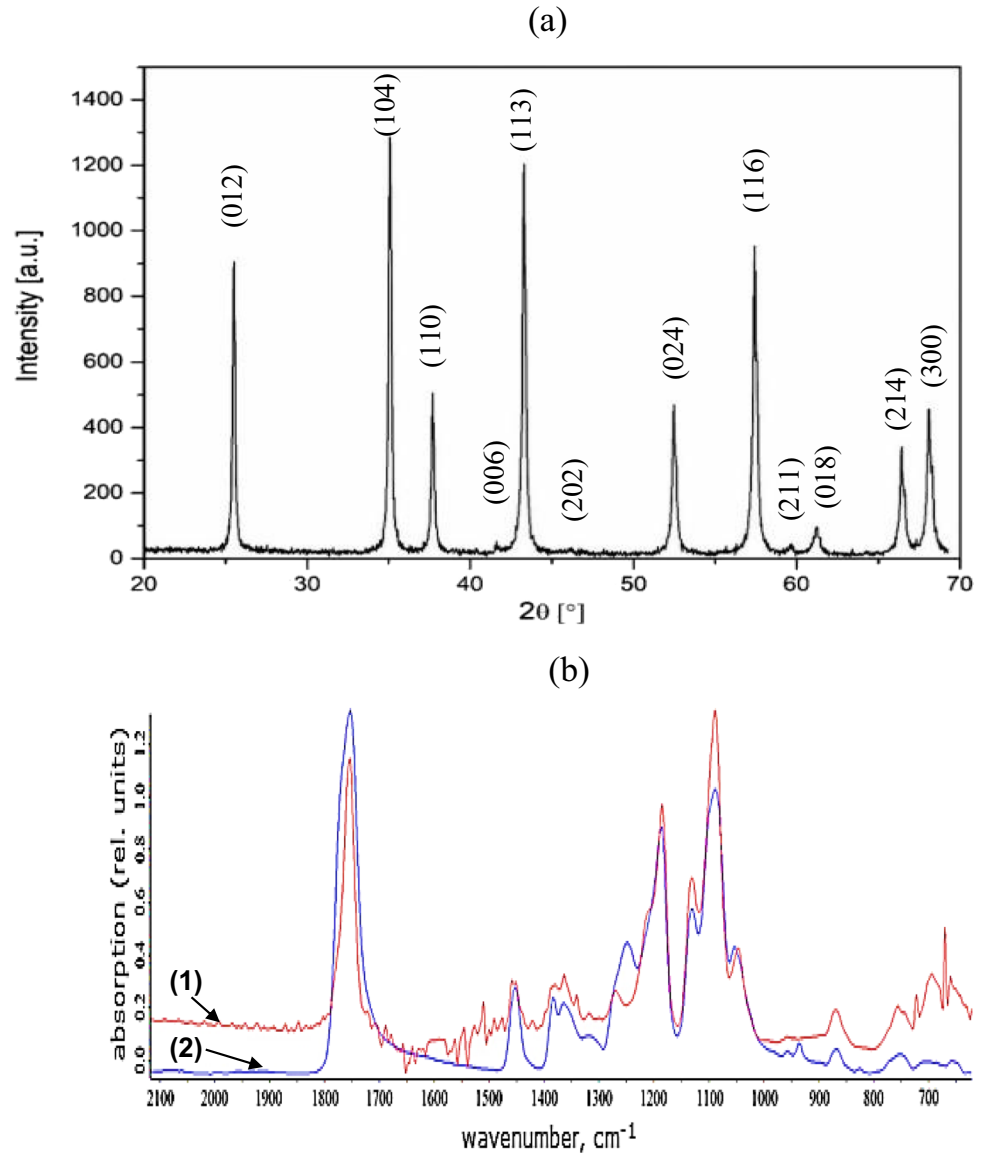
The X-ray diffraction pattern of Al₂O₃ powder is shown in Fig. 2a. The obtained results confirm that the initial ceramic powder corresponds to the alpha alumina phase (α -Al₂O₃). Based on the detection limit of XRD (0.5 to 2 molecular %), no secondary phases or impurities were observed. Figure 2b shows the IR spectrum of the PLA polymer powder (1) downloaded from the database (2). The result highlights that the main peaks of the spectrum downloaded from the database correspond to those of the initial powder, which allows us to conclude that the initial powder is a PLA.

Special requirements are applied to powder materials used in additive manufacturing technologies: particle sphericity as well as a narrow and uniform size distribution range. The content of particles larger than the permissible size or irregularly shaped particles should be determined with high accuracy since the presence of such particles affects all properties: rheological, thermal, reaction-kinetic characteristics, and mechanical properties of materials. They can also cause defects in the finished product. Therefore, the dispersion composition of the initial powders of Al₂O₃ and PLA binding as well as the shape of their particles were studied (Fig. 3). As can be seen in Fig. 3, the spherical particles predominate. Also, large, irregularly shaped inclusions are present in the PLA powder.

Therefore, it is necessary to conduct a granulometric analysis of both raw materials and composite compounds to compile a complete picture of the material properties. The objective was to obtain a homogeneous distribution of ceramic and polymer particles, to ensure their good mixing and extrusion, and to obtain a homogeneous ceramic-polymer filament. For this reason, the three ceramic-to-polymer ratios (by volume) were studied: 70% Al₂O₃/30% PLA, 60% Al₂O₃/40% PLA, and 50% Al₂O₃/50% PLA.

As follows from the obtained data (Table 1), the values in Al₂O₃-PLA compounds differ from those of raw materials. Even though spherical particles predominate in the

Fig. 2 **a** X-ray diffraction data of the initial powder Al_2O_3 ($\alpha\text{-Al}_2\text{O}_3$ peaks are indexed for the hexagonal system), **b** IR spectrum of the initial polylactic acid powder (1) and downloaded from the database (2)



compound, as in the initial powders, both irregularly shaped particles and small fractions are also present. This is due to the process of homogenization of compounds in a ball mill, during which, on the one hand, Al_2O_3 particles can be crushed. Consequently, the initially spherical Al_2O_3 particles became irregular and angularly shaped with a high specific surface area. At the same time, the PLA particles can change shape to a lamellar one. On the other hand, during mixing, aggregation of ceramic particles and polymer sticking to Al_2O_3 powders may occur, which leads to an increase in the average size of particles (Fig. 4).

Based only on the obtained results shown in Table 1, it can be assumed that 50%/50% and 60%/40% powder Al_2O_3 -PLA compounds are preferable for filament extrusion since their average particle size practically corresponds to the average particle size of the raw materials. However, a

larger average grain size in a 70%/30% powder Al_2O_3 -PLA composition may not provide compact stacking of particles in a certain volume and, accordingly, high density in the filament after extrusion, as well as powder fluidity with minimal resistance during extrusion. Note that the microstructural particle distribution of the 60%/40% Al_2O_3 -PLA compounds looks more uniform (Fig. 4b) compared to the other two (Fig. 4a, c).

3.2 Al_2O_3 -PLA filament fabrication

In order to check the quality of filament according to the composition, each mixture of Al_2O_3 -PLA was extruded using the Wellzoom bench-top extruder. Figure 5 shows photographs of the obtained ceramic-polymer filaments with Al_2O_3 content of 50%, 60%, and 70%. As can be

Fig. 3 Micrographie of initial powders obtained by scanning electron microscopy (SEM), **a** a general view of the initial powder Al_2O_3 ; **b** a particle of Al_2O_3 powder at a higher magnification; **c** a general view of the initial PLA powder; **d** a particle of PLA powder at a higher magnification

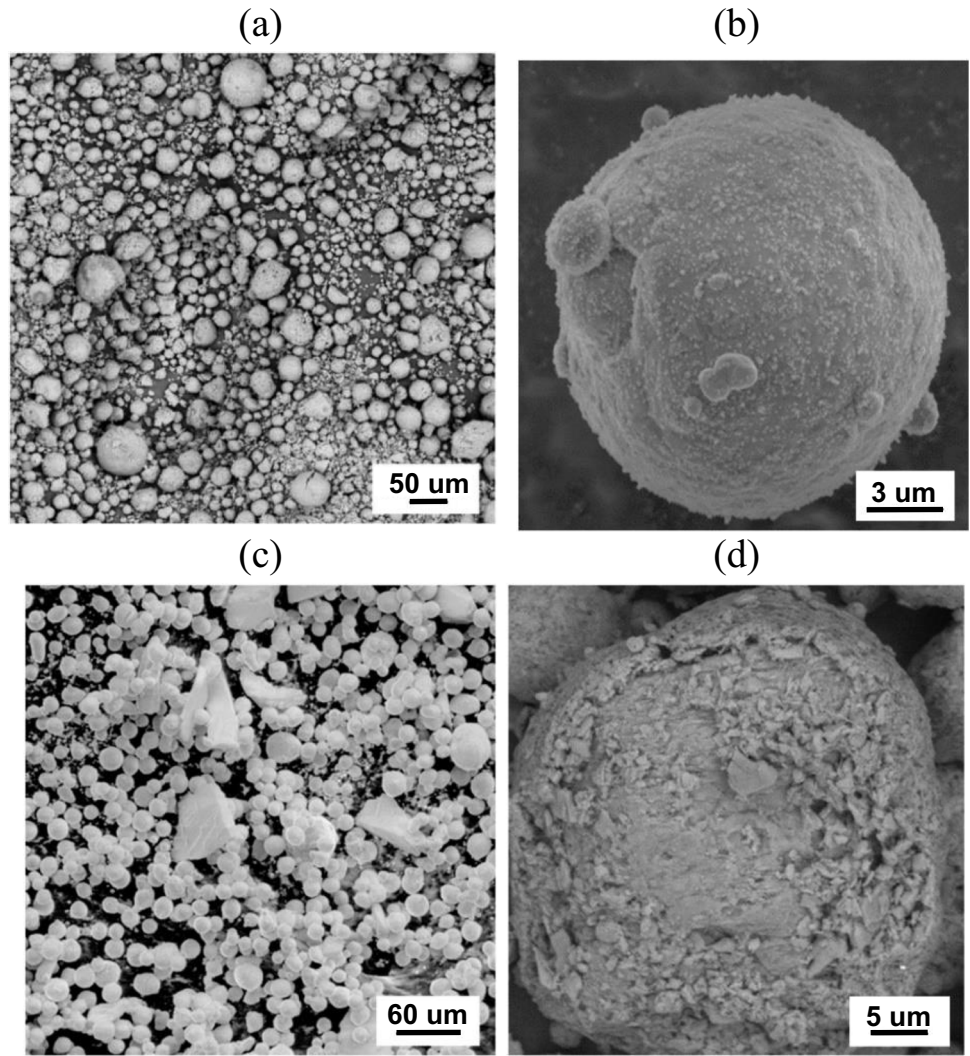


Table 1 Granulometric analysis of the initial PLA and Al_2O_3 powders and the mixtures obtained from them

Test samples	* d_5 , μm	* d_{50} , μm	* d_{95} , μm	d_{average} , μm	†Solidity, %	‡Circularity, %
Al_2O_3	15.5	34.3	69.1	36	97.2	81.1
PLA	17	35.2	48.9	35	93.1	74.9
50/50	13.2	32.9	93.3	38	77.4	72.9
60/40	16.8	35.3	96.2	35	80.4	78.6
70/30	23.6	44.1	19.4	44	81.9	79.3

* $d_5=15.5 \mu\text{m}$, $d_{50}=34.3 \mu\text{m}$, and $d_{95}=69.1 \mu\text{m}$ means that 5% of the powder is less than $15.5 \mu\text{m}$, 50% is less than $34.3 \mu\text{m}$, and 95% less is than $69.1 \mu\text{m}$

†This parameter shows the ratio of the particle area to the convex area closest to it. Particles with very smooth outlines will have a solidity value close to 1, while particles with rough outlines or agglomerated particles will have lower solidity values

‡This parameter denotes the proximity of the particle shape to a circle and is calculated by the formula S_c/S_e , where S_c is the area of the inscribed circle and S_e is the area of the equivalent circle

seen, the filaments with a ceramic content of 50 and 60%, respectively, did not have significant deviations from the shape, were well extruded, and turned out to be sufficiently flexible and visually integral. The filament with a ceramic

content of 70% (Fig. 5c) turned out to be the most brittle and not flexible enough to be wound around a spool for continuous feeding, with an inconsistent cross-sectional shape and the presence of visual structural defects (pores

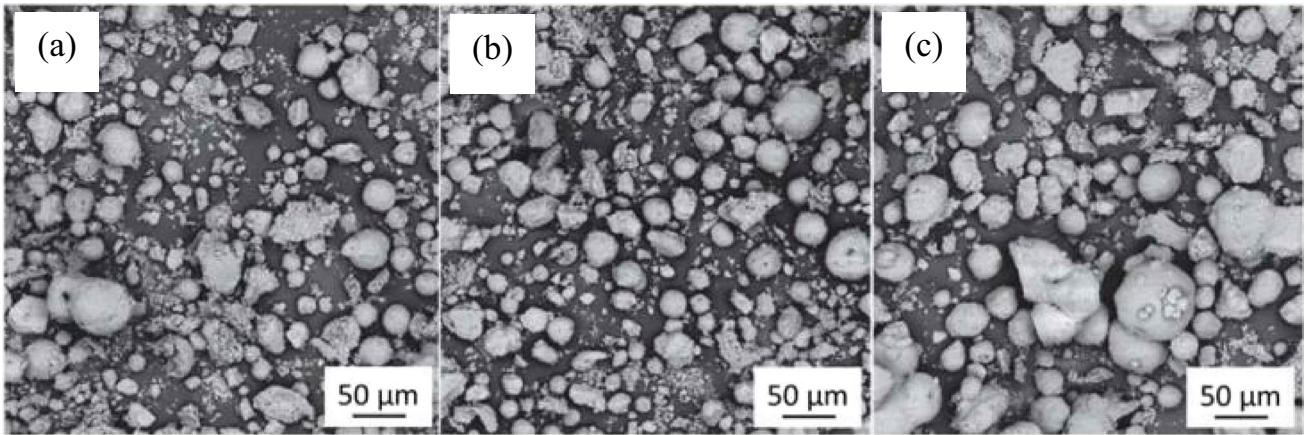


Fig. 4 Microstructure of $\text{Al}_2\text{O}_3/\text{PLA}$ mixtures obtained by scanning electron microscopy (SEM) equipped with a secondary electrons (SE) detector to obtain topographic contrast, and a backscattered electrons (BSE) detector to obtain compositional contrast with **a** 50%, **b** 60%, and **c** 70% of Al_2O_3 (by volume)

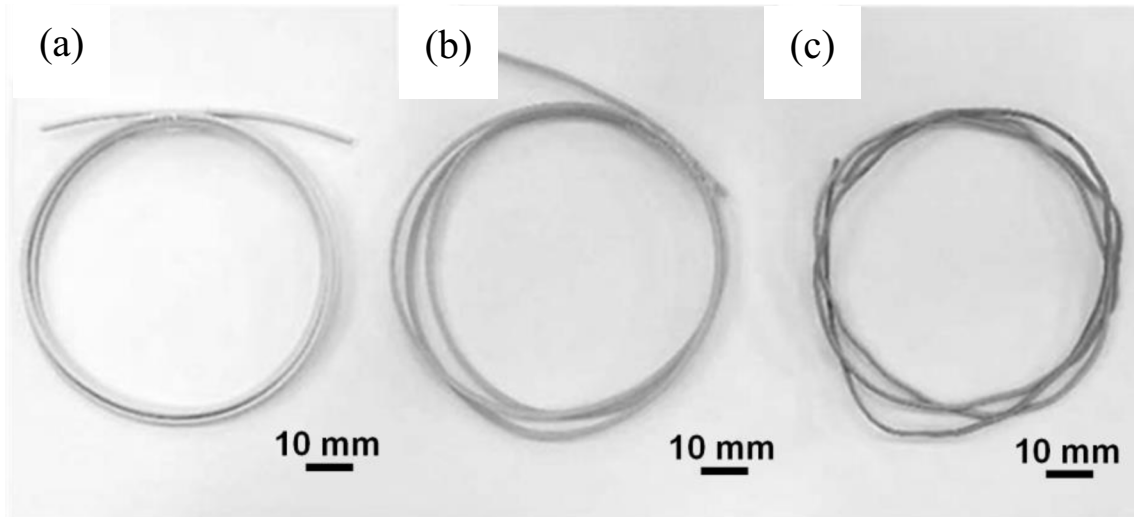


Fig. 5 Composite filament with diameter 1.7 ± 0.1 mm after extrusion. **a** 40% PLA/60% Al_2O_3 , **b** 50% PLA/50% Al_2O_3 , and **c** 30% PLA/70% Al_2O_3

and cracks) was poorly extruded, broke during extrusion, and clogged the extruder nozzle. The probable reason for such properties is the non-uniform distribution and larger particle sizes in the initial mixture, as indicated above. For the rest of the study, a 40% PLA/60% Al_2O_3 filament was chosen.

To ensure good printing quality, the average value of the cross-sectional diameters of the obtained filament varied in the range of 1.7 ± 0.1 mm. Note that it is very important to produce a filament with tight tolerances on the diameter, because the volumetric flow rate is based on the assumption that the filament has a constant diameter. If the filament diameter is smaller than the specific value,

Table 2 The results of measuring the density values of $\text{Al}_2\text{O}_3/\text{PLA}$ compounds of powders

Sample N ^o	Name of the compound	Theoretical density values, g/cm^3	True density values, g/cm^3
1	30% PLA + 70% Al_2O_3	3.09	3.10
2			3.09
3			3.10
1	40% PLA + 60% Al_2O_3	2.83	2.81
2			2.84
3			2.82
1	50% PLA + 50% Al_2O_3	2.57	2.55
2			2.56
3			2.58

Fig. 6 Frequency curves of the elastic modulus and loss modulus at the various temperatures for **a** unfilled PLA and **b** filled PLA with Al_2O_3 60%vol

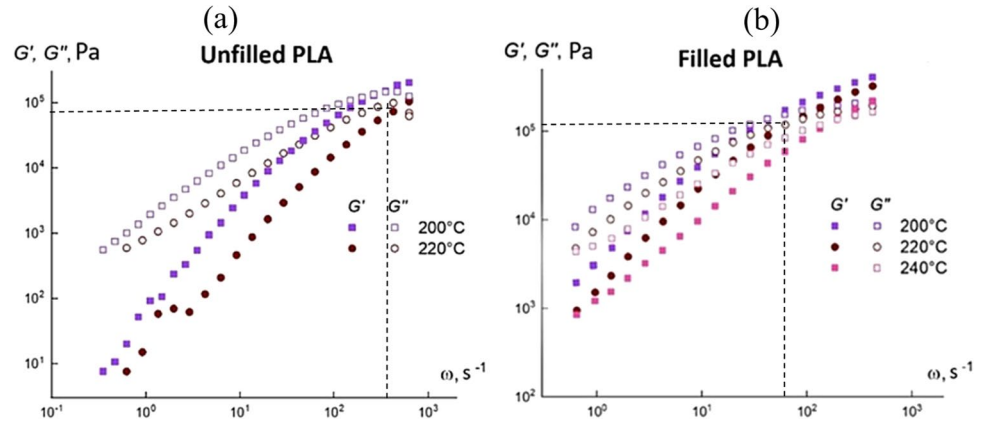


Table 3 Dependence of the thickness of the printed ceramic-polymer filament on the temperature and printing speed

Material	Print temperature, °C	Print speed, mm/s	Thickness of the printed filament, μm
40%PLA/60% Al_2O_3	190	1.25	572
		1.4	550
		2	583
	220	1.25	448
		1.4	468
		2	510
	250	1.25	385
		1.4	344
		2	333

the volumetric flow rate is lower, and therefore, the deposited extruded filament has smaller widths and thicknesses. This is referred to as underflow. The latter generates poor bonding between the deposited filaments or creates voids between adjacent filaments that will not be closed after the sintering process. Contrariwise, if the diameter is larger

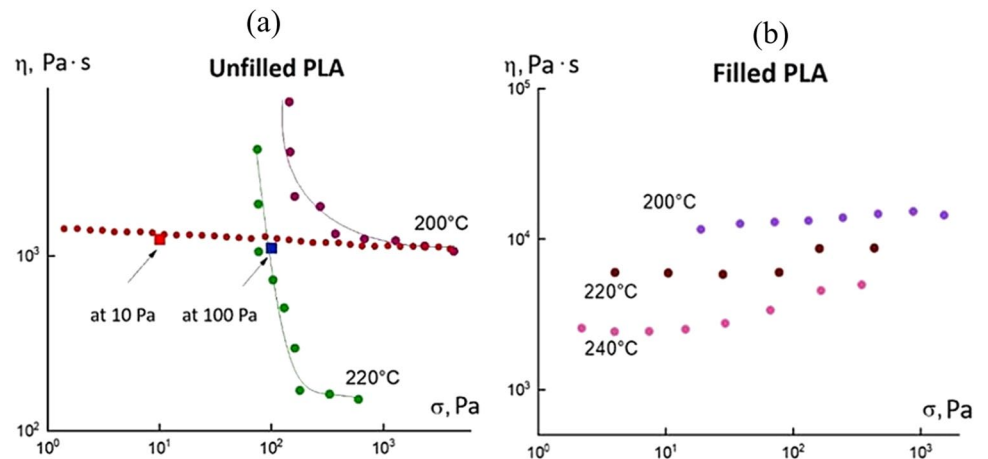
than the specific value, the extruded filament deposition may lead to overflow, which leads to a poor definition of the fine feature of the part.

The obtained results of the true density of $\text{Al}_2\text{O}_3/\text{PLA}$ compounds do not differ from the theoretical ones which indicate the absence of impurities in the initial components (see Table 2).

3.3 Rheological properties

The rheological properties of the promising composition must be acceptable to ensure appropriate flexibility and strength of the resulting filament to spool and de-spool it for storage and printing, respectively. It is also important to avoid obstructions in the nozzle and prevent defects during printing. In this context, the frequency curves of the elastic (or storage) modulus (G') and viscous (loss) modulus (G'') at the various temperatures for the unfilled and filled PLA with 60%vol Al_2O_3 are presented in Fig. 6. The study of the filled PLA showed that the rheological properties differ markedly from those of the unfilled PLA. Table 3 and Fig. 6b

Fig. 7 Complex viscosity (η) versus shear stress (σ) plot for the **a** unfilled PLA and **b** filled PLA at different temperatures



present the viscoelastic behavior of the filled PLA in the form of frequency dependences. In contrast to the unfilled PLA (Fig. 6a), the G' and G'' curves intersect at 60 s^{-1} at $220 \text{ }^\circ\text{C}$, above which elastic deformations predominate.

The crossover point at $220 \text{ }^\circ\text{C}$ corresponds to a modulus value of $1.1 \times 10^5 \text{ Pa}$, while for the unfilled PLA, it was found at a higher frequency of 400 s^{-1} to be $6.5 \times 10^4 \text{ Pa}$. Above this value, the elastic component of the dynamic modulus prevails over the loss modulus, which indicates that the elasticity of the material becomes dominant. Figure 7 shows graphs of the dependence of complex viscosity (η) on shear stress (σ) for unfilled and filled PLA at different temperatures.

As the temperature rises, the values of the modules are expected to decrease, and the crossover point shifts to the region of higher angular frequencies. Moreover, under stationary shear conditions (Fig. 7b), the filled PLA behaves like a Newtonian liquid with a viscosity of $7 \times 10^3 \text{ Pa}\cdot\text{s}$ at $220 \text{ }^\circ\text{C}$, which is approximately 6 times higher than the viscosity of the unfilled sample. Such an increase in viscosity is

due to the presence of a filler and the adsorption of polymer macromolecules on it. Based on the rheological properties, it is evident that the filled PLA is acceptable for the production of the filament by extrusion. It behaves as a Newtonian viscoelastic liquid with a viscosity much higher than that of unfilled PLA. This fact, along with decreased angle coefficients of frequency dependencies of the elastic and loss moduli, indicates the formation of a sufficiently strong structure in the composite.

3.4 Printing parameters

For exact printing results, the thickness of the printing filament must be within a very small tolerance range of the height layer parameter introduced in the slicer. For this purpose, the 60% Al_2O_3 /40% PLA compound was extruded at different temperatures and printing speeds. The starting point for searching optimal interval printing parameters was based on the optimized parameters of PLA filament [44]. The surface study of the 60% Al_2O_3 /40% PLA samples

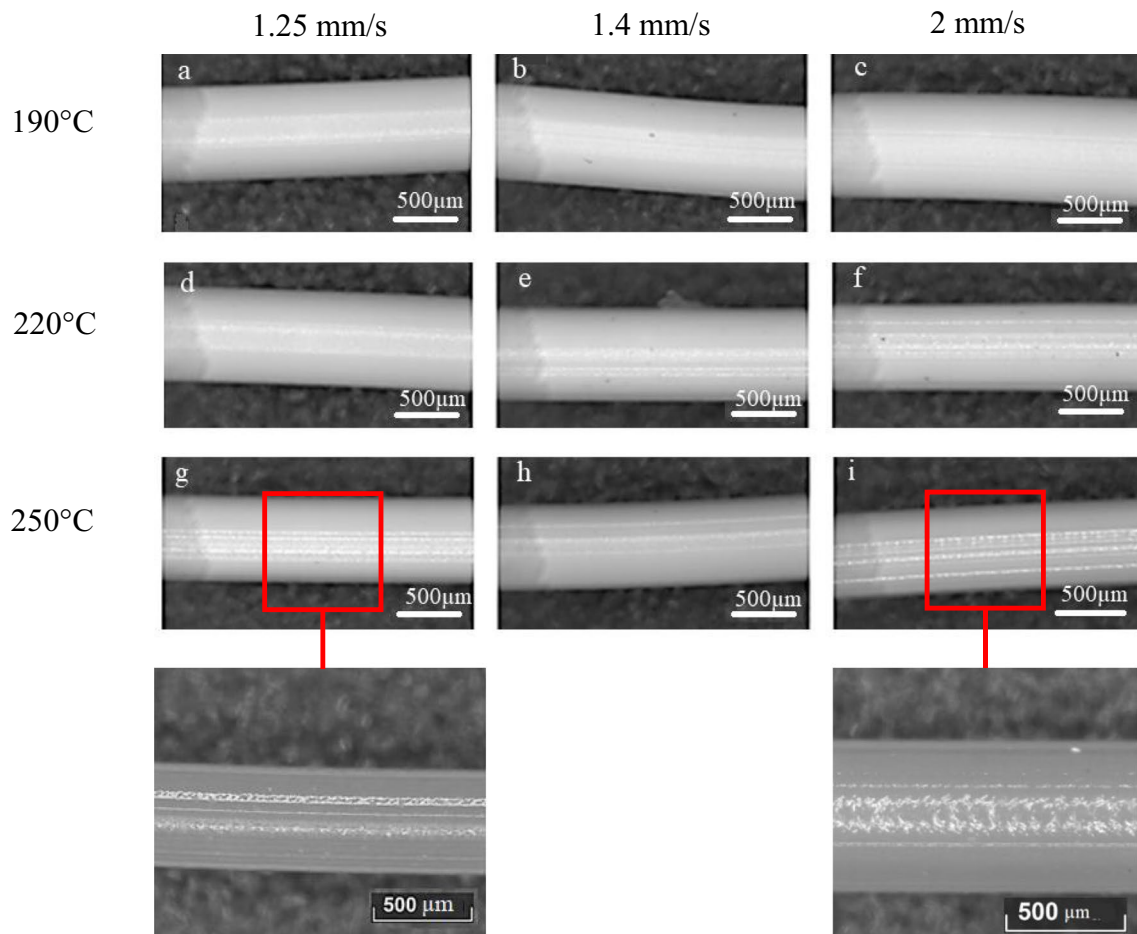


Fig. 8 Surface optical microphotographs study of the 60% Al_2O_3 /40% PLA filament obtained at a printing speed of 1.25 mm/s (a, d, g) and showing banding defect from $220 \text{ }^\circ\text{C}$, 1.4 mm/s (b, e, h), and 2 mm/s (c, f, i) and showing shark skin defect from $220 \text{ }^\circ\text{C}$

Table 4 Printing parameters for alumina material using FFFC technology

Parameters	Al ₂ O ₃ /PLA filament
Printing speed	1.4 mm/s
Filament extrusion multiplier	1
Printing temperature	220 °C
Bed temperature	70 °C
Layer height	0.2, 0.3, and 0.4 mm
Infill density	100%
Nozzle diameter	0.6 or 0.8 mm
Overlap	30%
Infill pattern	Rectilinear

shows that at different temperatures and printing speeds, the filaments have different surface quality (Fig. 8) and thickness (Table 3). The temperature strongly affects the filament thickness; the higher the printing temperature, the thinner the filament in most cases. Varying the printer speed was not clear about sample thickness, but it was found to influence defect formation. At low printing speeds (~1.25 mm/s), banding was formed in the samples, whereas at the highest speeds (~2 mm/s), a “shark skin” defect was observed.

Based on the obtained results, the following printing parameters were chosen for the 40% PLA/60% Al₂O₃ samples corresponding to the printing temperature of 220 °C, the printing speed of 1.4 mm/s, the layer height of 0.4 mm, and the bed temperature of 70 °C (see Table 4).

3.5 Binding removal and sintering

After printing, the so-called green part undergoes the thermal debinding cycle. At this stage, the idea is to be able to remove the organic binder component without any residue and yet leave the sample without any structural damage.

Table 5 Debinding and sintering process parameters

Segment	Time, min	Change in temperature, °C		Heating rate, °C/min	
		From	To		
1	30	20	60	0.5	Debinding
2	30	60	60	0	
3	30	60	70	0.5	
4	220	70	170	0.5	
5	60	170	170	0	Sintering
6	160	170	250	0.5	
7	60	250	250	0	
8	700	250	600	0.5	
9	60	600	600	0	
10	475	600	1550	2	
11	120	1550	1550	0	

For that, a thermogravimetric analysis (TGA) of the filament was conducted (Fig. 9). The tests were carried out in a heating mode at a constant rate of 1 °C/min in the range of 25 to 1000 °C in an air atmosphere. The heating rate of the debinding thermal cycle was limited to 0.5 °C/min. However, if the debinding process is too fast, above 10 °C/min, it can lead to cracks, deformation, and, in the worst case, loss of structural integrity of the part. This low heating rate constraint is a consequence of using only one polymeric material as binding. It generates a very slow process compared to solvent or catalytic debinding [41, 42]. Note that the filler shifts the decomposition temperature to a higher temperature.

Table 5 shows the debinding and sintering cycles applied. The exposure at the first temperature ($T = 60$ °C) corresponds to the softening temperature of the polylactic acid. The next exposure corresponds to the glass transition temperature of the polymer ($T = 70$ °C), followed

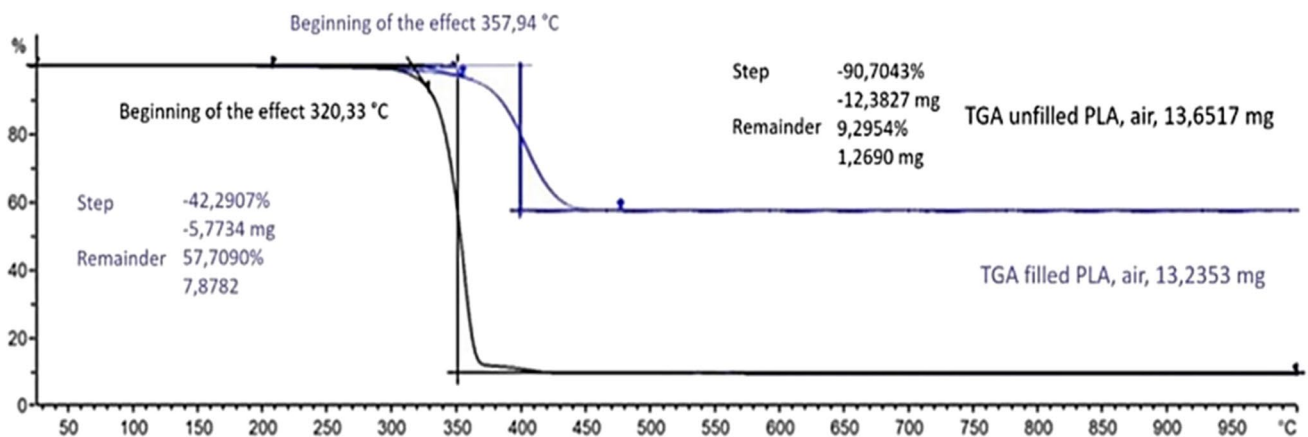


Fig. 9 Thermogravimetric curve of the filled and unfilled PLA

by the melting temperature ($T = 170\text{ }^{\circ}\text{C}$). $T = 250\text{ }^{\circ}\text{C}$ explains the beginning of thermal oxidation of the polylactic acid and allows it to be burned out equally, preventing its boiling, which can lead to the destruction of the ceramic frame of the sample. The maximum rate of thermal oxidation of PLA is reached at a temperature of $300\text{ }^{\circ}\text{C}$. The process was continued to $600\text{ }^{\circ}\text{C}$ at the same heating rate to finally burn out the polymer. After the debinding process, solid-state sintering was used to achieve the final densified part. During the process, the so-called brown part is heated to a temperature that is typically between 0.5 and 0.8 of the melting temperature [51]. When the sintering temperature and holding time increase, the alumina particles bond with each other, the particles grow, and the pores gradually decrease. The elimination of the solid–gas interface and its replacement by the solid–solid interface is the dominant mechanism that ensures the forming and reshaping of the powder [52]. In this study, the thermal debinding and sintering cycles were processed in an electric furnace SNOL 1.7/1700 (AB Umega, Lithuania) under air conditioning. Subsequent heating up to $600\text{ }^{\circ}\text{C}$ for 1 h and exposure at a maximum temperature of $1550\text{ }^{\circ}\text{C}$ for 2 h led to the final burning of PLA and the sintering of ceramics.

A study of the microstructure of the sintered ceramic samples showed the presence of pores on the surface of the materials formed due to the removal of the polymer binder. Figure 10a shows the characteristic microstructure of all experimental samples. When determining the elemental analysis by the EDX method (Fig. 10b), it was found that the samples contain on average 56% oxygen and 44% aluminum in mass proportion. The presence of carbon was not detected on any of the spectra, which indicates the possibility of

complete polymer burning out under the considered heat conditions.

The mean value of the measured density of sintered parts was obtained at 3.75 g/cm^3 . This value is close to the bulk density of alumina (3.95 g/cm^3), but the difference is in the degree of porosity observed in 3D-printed parts. SEM analysis presented in Fig. 10a shows the presence of vermicular formations in the ceramic phase with numerous spherical and non-spherical pores. The porosities observed in specimens obtained by the FFF process when working with semi-crystalline polymers and highly filled composite filaments are common and constitute a drawback of the process.

In the FFF process, the temperature of the deposited layer is often lower than the next one. Hence, the adhesion between new and previously deposited layers is dependent on the diffusion of the polymer chain across the interface and related to the residual thermal stress distribution. These phenomena are directly influenced by several parameters such as viscosity, temperature, surface tension, and the thermal mismatch between deposited materials [52–54]. The shape of porosity can help us obtain information on the source of determination. In our case, the spherical pores observed are related to thermal treatment (debinding and sintering), whereas the non-spherical ones are FFF-process induced [55, 56].

The dimensions of each printed sample were measured after sintering and compared to those of “green” samples (Fig. 11). The shrinkage was not isotropic, as it was $\sim 23\%$ in the Z direction and $\sim 15\%$ in the radial direction. In the Z direction, the value found was in line with those found by other authors using the FFF process [57–59], whereas in X and Y directions, literature reports approximately 17–20%

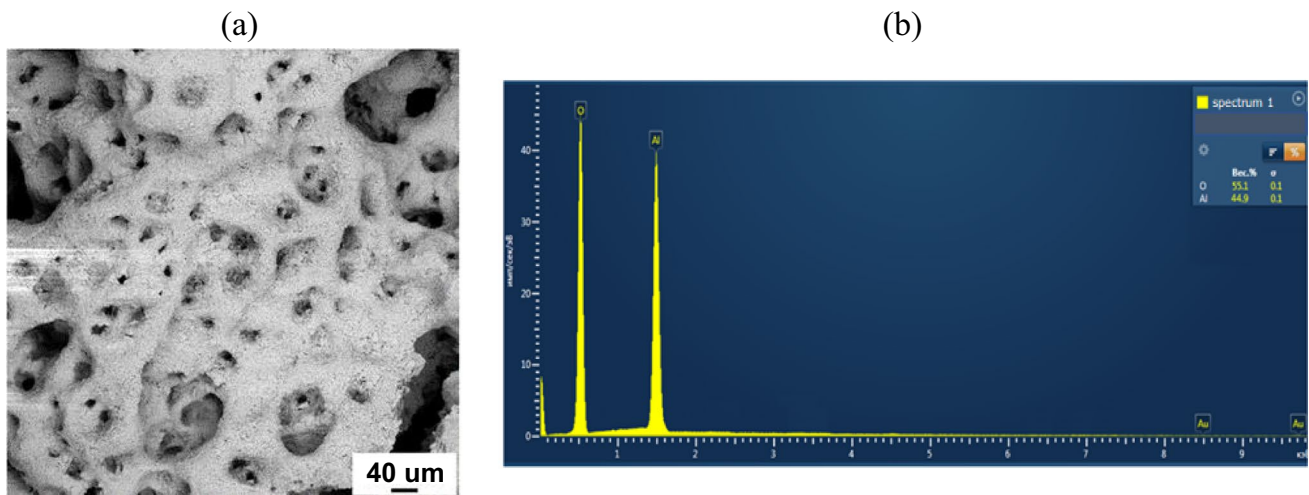


Fig. 10 **a** The ceramic structure after the complete heat treatment program; **b** The characteristic spectrum of the material after burning the polymer binder obtained by the EDX method

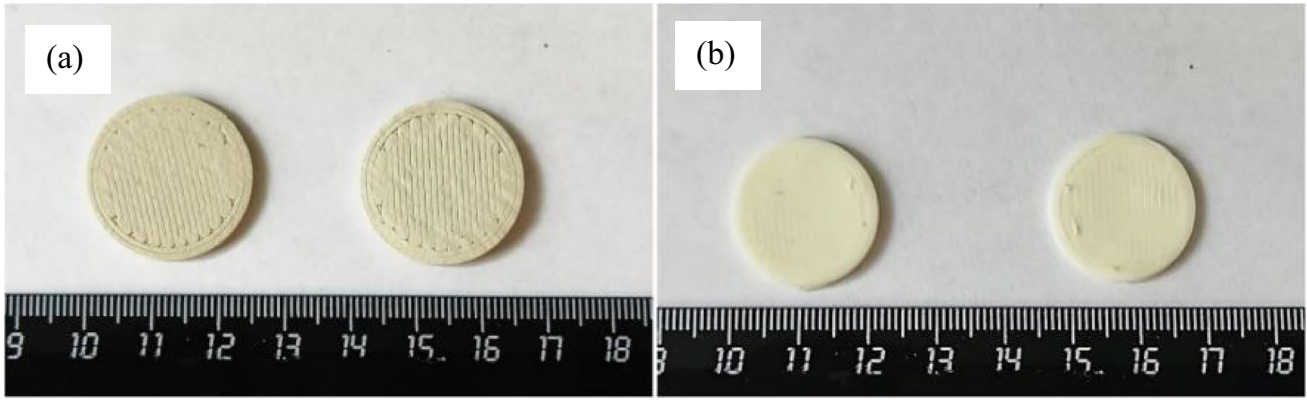


Fig. 11 Alumina printed samples, **a** “green” samples, **b** sintering samples for the bending test

Table 6 Density and average shrinkage properties of alumina 3D-printed parts using FFF process

References	Relative density (%)	Average shrinkage (%)
Current study	91	23 (z), 15 (plane)
Tosto et al. [57]	95	22.9 (z), 20.7 (xy)
Nötzel et al. [58]	97	20.75
Gorjan et al. [59]	98	23 (z), 17 (plane)
Orlovska et al. [29]	86–89	19

assuming a relative density of 95–98% (see Table 6). This difference is explained by the fact that our samples are not fully densified after sintering. The relative density of the 3D sintered samples was about 91%.

To test the capacity of 40% PLA/60% Al_2O_3 filament to print complex geometries with fine features and moderate overhangs, two complex parts were printed using a 0.4-mm nozzle and a 0.2-mm high layer. The final ceramic products obtained before and after debinding and sintering cycles are presented in Fig. 12.

3.6 Mechanical characterization

Figure 13 shows the tensile properties of unfilled and filled PLA filaments (40% PLA/60% Al_2O_3) of 3D printed samples. On the one hand, the analysis of the obtained curves shows the uniform behavior of the samples printed from unfilled PLA, which indicates greater homogeneity of the printed samples. On the other hand, the 3D-printed specimens made of 40% PLA/60% Al_2O_3 have a plastic domain smaller than unfilled PLA (i.e., a shorter stress–strain curve); however, the stiffness increases slightly. Note that the distribution of Al_2O_3 powder in the PLA influences the mechanical behavior of the filament.

To understand how the geometric infill affects the biaxial fracture strength of sintered samples, several infill configurations (line, concentric, and zigzag) with layer heights of 0.2 mm, 0.3 mm, and 0.5 mm were applied. All materials show a brittle behavior typical for ceramics, with no plastic deformation. It can be seen from the results presented that the printed samples with the filling type “line” and a layer height of 0.4 mm have better mechanical properties. This can be explained by the fact that the fewer horizontal layers in the sample, the fewer voids there are, which negatively affect the mechanical behavior. Also, the higher the line thickness, the fewer horizontal layers need to be extruded before reaching a given disc height, and, accordingly, fewer voids are formed in the printed object. When printing an object with the fill type “line,” a two-dimensional grid is created in which one layer prints along one axis only. For the examined sample shape and the filling density of 100%, this filling type allowed the slicer software to place the extruded filaments with the maximum possible contact between them, in contrast to the “zigzag” and “concentric” filling patterns. To better understand the geometrical infill effect on mechanical properties, a multi-scale surface characterization including porosity is recommended [60]. The maximum strength value was 332 ± 21 MPa, which is only 53 MPa lower than that of corundum ceramics made by pressure-free sintering (Fig. 14). It should be noted that the flexural strength of alumina is highly dependent on the manufacturing process. Pressure-free sintering of high-purity alumina with a relative density of less than 99% reaches 520 MPa [61], whereas robocasting achieves a flexural strength value of ~ 156 up to 350 MPa [17, 62]. In the FFF printing of alumina, Orlovska et al. [29] obtained flexural strengths of 300 and 200 MPa depending on layer heights, whereas Truxová et al. [63] obtained 331 MPa, while a range of 200–500 MPa was claimed by the manufacturer. The flexural strength difference observed has its origin in the mechanics of ceramics. The presence of

Fig. 12 Complex parts fabricated from 40% PLA/60% Al_2O_3 filament using Black Widow 3D printer. **a-c** Drill and impeller green parts, and **b-d** drill and impeller sintered parts

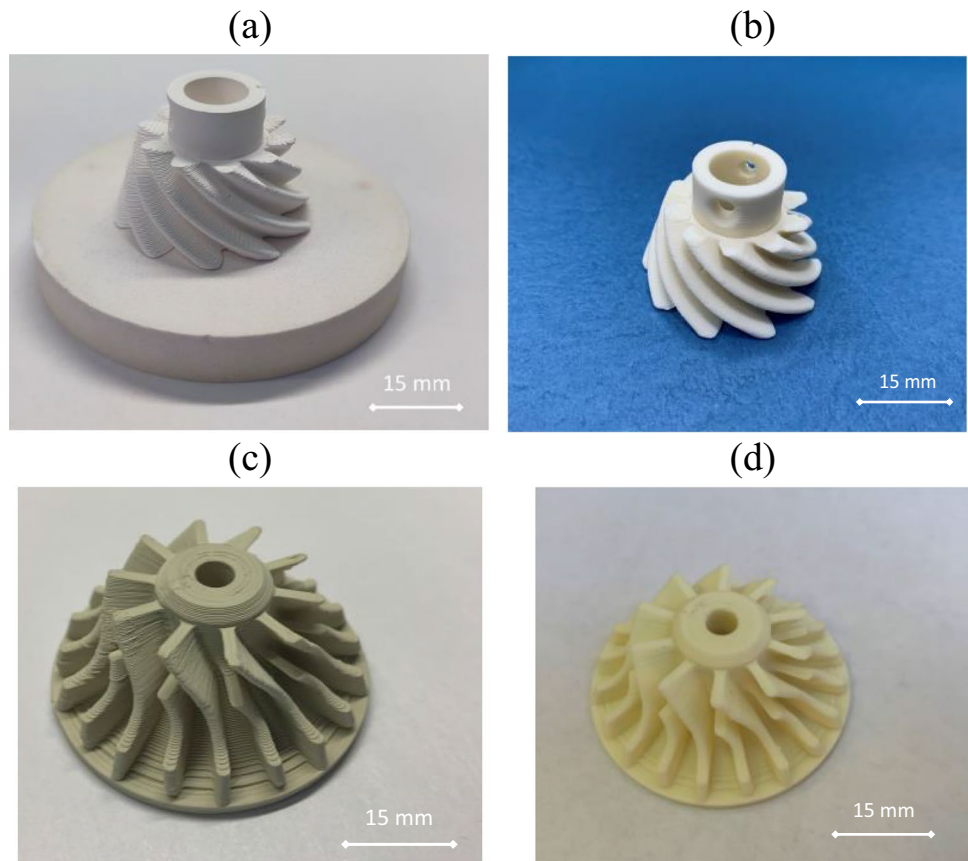
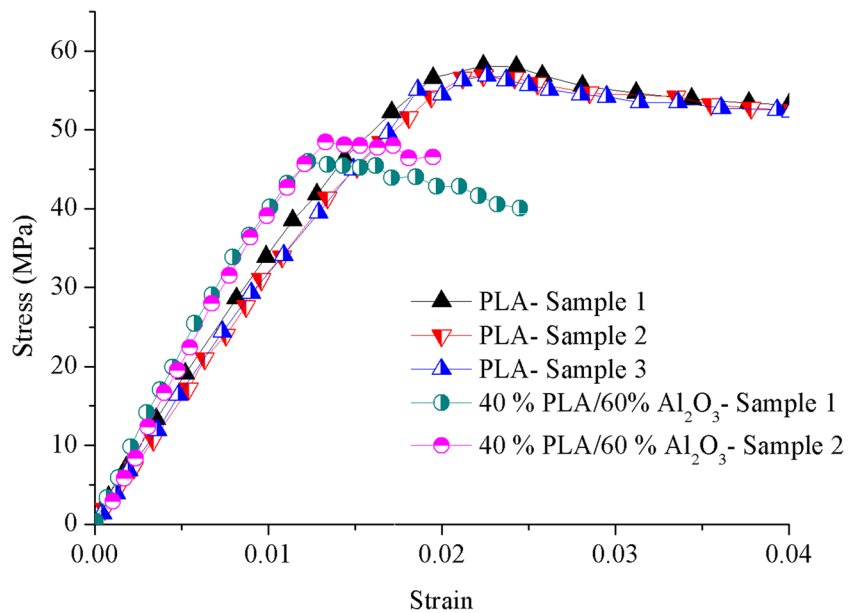


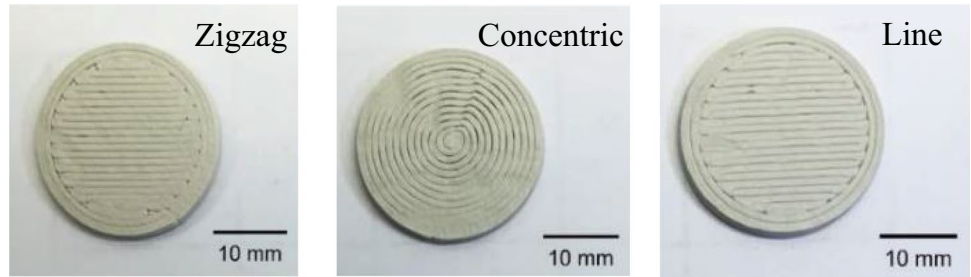
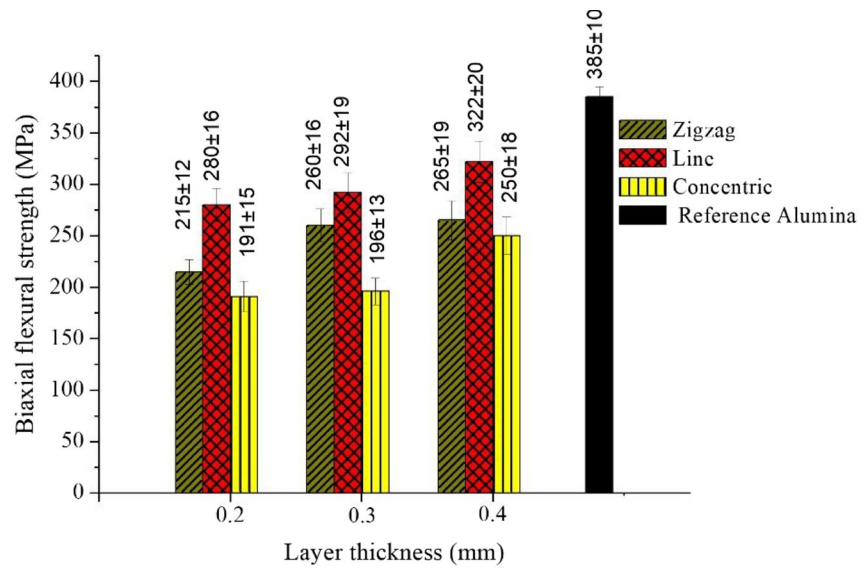
Fig. 13 Tensile properties of unfilled (PLA) and filled (40% PLA/60% Al_2O_3) filaments of 3D printed samples



porosity at both nano and micro sizes highly influences the growth of cracks, leading to premature failure. As shown by the SEM investigation (see Fig. 10a), there are

numerous spherical and non-spherical pores in the studied samples as a consequence of the FFF process. These porosities act as defects, lowering mechanical properties.

Fig. 14 Biaxial flexural strength of sintered alumina disks printed with a 0.6-mm diameter nozzle as function of layer thickness for several infill geometries



3.7 Discussion

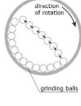
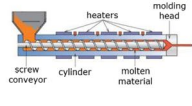


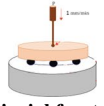
The main results obtained in the study are summarized in Table 7, including all the important information from the result section to give a better idea of the whole picture of the adapted strategy. As follows from the presented values, it was not possible to obtain sintered ceramic samples with high density and strength. To increase these values, it is intended to modify the original aluminum oxide powder using the spray drying method to give the particles a spherical shape of multimodal size. The small particles will fill the voids between the coarse particles, providing a dense packing of particles and a high degree of solid phase filling of the raw material. It is expected that the spherical multi-size particles will be more densely packed, which should lead to the formation of a denser microstructure in the printed object, thus improving the properties of the sintered ceramic sample. In addition, it is possible to further replace the polymer base with a polymer of linear structure containing no aromatic fragments or unsaturated C–C bonds to avoid its coking at high temperatures during debinding and sintering, and obtain a defect-free ceramic sample.

4 Conclusion

The present study has demonstrated the feasibility of producing a low-cost ceramic-polymer filament for the FFFC process based on micrometric alumina (Al_2O_3) powder and polylactic acid (PLA) polymer as the binder system without any additive. To ensure the Al_2O_3 /PLA mixture had a homogeneous particle distribution, the colloidal method was chosen, and from that, a customized way to produce filament and samples was adapted. The choice of alumina material is motivated by its low cost, availability, and use in various industries of mechanical engineering, automobile, and aircraft construction, as well as in biomedical applications, whereas PLA is chosen for its easier printing process and its biodegradability and biocompatibility. Based on the experimental results obtained in this work, the following conclusions could be drawn:

- Among the three studied mixtures, it would seem that 60% Al_2O_3 /40% PLA provides enough viscosity and flow ability when in the molten state and enough mechanical strength for handling and processing the

Table 7 Summary of the study including all the important information from the result section to give a better idea on the whole picture of the strategy, and give some suggestions on the optimization of the manufacture process

Technological chain adapted				Mechanical Characterization
				
Grinding in ball mill and drying the raw powders	Extrusion into ceramic-polymer filament	Printing of ceramic-polymer samples	Thermal debinding and sintering	Biaxial fracture strength (MPa)
30% PLA + 70% Al ₂ O ₃	<ul style="list-style-type: none"> • Brittle and not flexible • Presence of visual structural defects (pores and cracks) • Significant deviations from the shape 	<ul style="list-style-type: none"> • Not able to print 	N/A	N/A
40% PLA + 60% Al ₂ O ₃	<ul style="list-style-type: none"> • Well extruded and flexible • No significant deviations from the shape 	<ul style="list-style-type: none"> • Able to print (best composition) 	Not chemical debinding, only thermal debinding	<ul style="list-style-type: none"> • From 191 to 322[†]
50% PLA + 50% Al ₂ O ₃	<ul style="list-style-type: none"> • Well extruded and flexible • No significant deviations from the shape 	<ul style="list-style-type: none"> • Able to print (not tested in this study) 	N/A	N/A
The process parameters used				
<ul style="list-style-type: none"> • Al₂O₃ (d₅₀ ~ 40µm) • PLA (d₅₀ ~ 35µm) 	<ul style="list-style-type: none"> • Extrusion temperature : 220°C • Filament diameter [†]: 1.7 ± 0.1mm 	<ul style="list-style-type: none"> • Printing speed[†]: 1.4 mm/s • Printing temperature: 220°C 	<ul style="list-style-type: none"> • Debinding cycle[‡]: Heating from 20°C to 600°C at 0.5°C/min • Sintering cycle[‡]: Heating from 600°C to 1550°C at 2°C/min 	<ul style="list-style-type: none"> • Crosshead speed: 1 mm/min
<ul style="list-style-type: none"> • Mixture time: 24 hours • Mixture speed: 125 rpm • Drying temperature: 90°C • Drying time: 24 hours 		<ul style="list-style-type: none"> • Bed temperature: 70°C • Nozzle diameter[‡]: 0.6 mm • Infill pattern*: rectilinear 		
Suggestions on the optimization of the manufacture process				
	[†] obtained for 40% PLA + 60% Al ₂ O ₃ and 50% PLA + 50% Al ₂ O ₃ compositions.	[†] Varying the printer speed was found to influence defect formation. At printing speed ~ 1.25 mm/s, the banding was formed in the sample. For printing speed ~ 2 mm/s a “shark skin” defect was observed. [‡] Possible to use nozzle diameter of 0.4 mm * Concentric and zigzag pattern induce more porosities and less dimensional accuracy than rectilinear.	^{†,‡} See Table 5 for more details	[†] it depends on process parameters. See Fig 14. The maximum obtained relative density was 91%.
	<ul style="list-style-type: none"> • The used parameters in this study are obtained by trial error method. To take advantage, it is important to optimize the parameters of each step using for example design for experiment (DOE). • To increase the relative density and the strength values, it is intended to modify the original Al₂O₃ powder using the spray drying method to give the particles a spherical shape of multimodal size. 			

material before printing (melting state) and after printing (solidification state).

- The successful printing of specimens and complex parts using a standard nozzle of 0.4 up to 0.8 mm demonstrates that it is possible to use a binder system with only one polymeric material without additive need.
- Although the specimens present defects and significant porosities, the flexural strength value of 332 ± 21 MPa

is comparable with results obtained in the literature and may be sufficient for several technical applications.

To reduce the porosity of alumina samples and, hence, enhance their mechanical properties, it will be necessary to optimize the rheological properties of the mixture, printing parameters, and heat treatment cycle. For this purpose, it is supposed to modify the shape of the initial particles of

ceramic powder and use a new polymeric base (linear structure polymer). To detect and eliminate defects in the ceramic products of complex shape with the required characteristics, made using the FFFC method with highly filled ceramic-polymer filaments, topological optimization methods will be used to identify an arbitrary number of defects, their geometry, and their location in the 3D structure. It is planned to conduct mathematical modeling of the influence of characteristic defects appearing during layer-by-layer deposition printing at different types filling of the 3D model on the mechanical properties of the samples. Furthermore, it is planned to assess the influence of typical defects arising from FFFC at different filling patterns of a 3D model on the mechanical properties of samples. Finally, we believe that the customized technological chain adapted could be readily applied to other ceramic materials and opens a way towards the democratization of the use of technical ceramics at a lower cost in everyday use and for specific technical applications.

Author contribution A. Smirnov: investigation, data curation, software, conceptualization, funding acquisition, supervision. S. Terekhina: methodology, writing—original draft preparation. T.V. Tarasova: investigation, methodology, writing—original draft, validation. M.L. Hattali: methodology, writing—original draft preparation, reviewing and editing. S.N. Grigoriev: validation, writing—reviewing.

Funding This work was supported by the Ministry of Science and Higher Education of the Russian Federation under project 0707-2020-0034. This work was carried on the equipment of the Collective Use Center of MSTU “STANKIN” (project No. 075-15-2021-695).

Data availability The data that support the findings of this study are available from the corresponding author, upon reasonable request.

Declarations

Conflict of interest The authors declare no competing interests.

References

1. Matizamhuka WR (2018) Advanced ceramics—the new frontier in modern-day technology: Part I. *J S Afr Inst Min Metall* 118:757–764
2. Somiya S (1991) A review of advanced technical ceramics. *Mater Manuf Proc* 6(2):365–367. <https://doi.org/10.1080/10426919108934763>
3. Reza Rezaie H, Beigi Rizzi H, Rezaei Khamseh M, Öchsner A (2020) 3D-printing technologies for dental material processing. In: A review on dental materials. *Adv Struct Mater* 123. https://doi.org/10.1007/978-3-030-48931-1_6
4. Hattali ML, Valette S, Ropital F, Mesrati N, Tréheux D (2012) Interfacial behaviour on Al₂O₃/HAYNES® 214™ joints fabricated by solid state bonding technique with Ni or Cu–Ni–Cu interlayers. *J Eur Ceram Soc* 32(10):2253–2265
5. Sharma A, Babbar A, Tian Y et al (2022) Machining of ceramic materials: a state-of-the-art review. *Int J Interact Des Manuf*. <https://doi.org/10.1007/s12008-022-01016-7>
6. Sharma A, Kalsia M, Uppal AS, Babbar A, Dhawan V (2022) Machining of hard and brittle materials: a comprehensive review. *Mat Today: Proc* 50(5):1048–1052. <https://doi.org/10.1016/j.matpr.2021.07.452>
7. Klocke F (1997) Modern approaches for the production of ceramic components. *J Eur Ceram Soc* 17:457–465
8. Olhero SM, Torres PMC, Mesquita-Guimarães J, Baltazar J, Pinho-da-Cruz J, Gouveia S (2022) Conventional versus additive manufacturing in the structural performance of dense alumina-zirconia ceramics: 20 years of research, challenges and future perspectives. *J Manuf Process* 77:838–879
9. Sova A, Okunkova A, Grigoriev S, Smurov I (2012) Velocity of the particles accelerated by a cold spray micronozzle: experimental measurements and numerical simulation. *J Therm Spray Technol* 22:75–80. <https://doi.org/10.1007/s11666-012-9846-y>
10. Gusarov AV, Grigoriev SN, Volosova MA, Okunkova AA (2018) On productivity of laser additive manufacturing. *J Mater Process Technol* 261:213–232. <https://doi.org/10.1016/j.jmatprotec.2018.05.033>
11. Gmeiner R, Mitteramskogler G, Stampfl J, Boccaccini AR (2015) Stereolithographic ceramic manufacturing of high strength bioactive glass. *Int J Appl Ceram Technol* 12:38–45. <https://doi.org/10.1111/ijac.12325>
12. Sing SL, Yeong WY, Wiria FE, Tay BY, Zhao Z, Zhao L, Tian Z, Yang S (2017) Direct selective laser sintering and melting of ceramics: a review. *Rapid Prototyp J* 23:611–623. <https://doi.org/10.1108/RPJ-11-2015-0178>
13. Grossin D, Montón A, Navarrete-Segado P, Özmen E, Urruth G, Maury F, Maury D, Frances C, Tourbin M, Lenormand P, Bertrand G (2021) A review of additive manufacturing of ceramics by powder bed selective laser processing (sintering/melting): calcium phosphate, silicon carbide, zirconia, alumina, and their composites. *Open Ceram* 5:100073. <https://doi.org/10.1016/j.oceram.2021.100073>
14. Smurov I, Doubenskaia M, Grigoriev S et al (2012) Optical monitoring in laser cladding of Ti6Al4V. *J Therm Spray Technol* 21:1357–1362. <https://doi.org/10.1007/s11666-012-9808-4>
15. Khmyrov RS, Grigoriev SN, Okunkova AA, Gusarov AV (2014) On the possibility of selective laser melting of quartz glass. *Phys Proc* 56:345–356. <https://doi.org/10.1016/j.phpro.2014.08.117>
16. Finke B, Hesselbach J, Schütt A, Tidau M, Hampel B, Schilling M, Kwade A, Schilde C (2020) Influence of formulation parameters on the freeform extrusion process of ceramic pastes and resulting product properties. *Addit Manuf* 32:101005. <https://doi.org/10.1016/j.addma.2019.101005>
17. Maillard M, Chevalier J, Gremillard L, Baeza GP, Courtial EJ, Marion S, Garnier V (2022) Optimization of mechanical properties of robocast alumina parts through control of the paste rheology. *J Eur Ceram Soc*. <https://doi.org/10.1016/j.jeurceramsoc.2022.12.008>
18. Onagoruwa S, Bose S, Bandyopadhyay A (2001) Fused deposition of ceramics (FDC) and composites. *Sch Mech Mater Eng* 224–231. <https://doi.org/10.1117/1.2114788>
19. Bellini A, Shor L, Guceri SI (2005) New developments in fused deposition modeling of ceramics. *Rapid Prototyp J* 11:214–220. <https://doi.org/10.1108/13552540510612901>
20. Safai L, Cuellar JS, Smit G, Zadpoor AA (2019) A review of the fatigue behaviour of 3D printed polymers. *Adv Manuf* 28(87):97. <https://doi.org/10.1016/J.ADDMA.2019.03.023>
21. Terekhina S, Tarasova T, Egorov S et al (2020) On the difference in material structure and fatigue properties of polyamide specimens produced by fused filament fabrication and selective laser sintering. *Int J Adv Manuf Technol* 111:93–107. <https://doi.org/10.1007/s00170-020-06026-x>

22. Kariz M, Sernek M, Obucina M, Kuzman MK (2018) Effect of wood content in FDM filament on properties of 3D printed parts. *Mater Today Commun* 14:135–140
23. Khatri B, Lappe K, Noetzel D, Pursche K, Hanemann T (2018) A 3D-printable polymer-metal soft-magnetic functional composite—development and characterization. *Mater* 11:189
24. Terekhina S, Egorov S, Tarasova T, Skorniyakov I, Guillaumat L, Hattali ML (2022) In-nozzle impregnation of continuous textile flax fiber/polyamide 6 composite during FFF process. *Compos A: Appl Sci Manuf* 153:1. <https://doi.org/10.1016/j.compositesa.2021.106725>
25. Cao D, Malakooti S, Kulkarni VN, Ren Y, Lu H (2021) Nanoindentation measurement of core–skin interphase viscoelastic properties in a sandwich glass composite. *Mech Time-Depend Mater* 25:353–363. <https://doi.org/10.1007/s11043-020-09448-y>
26. Cao D (2023) An investigation on surface coated continuous flax fiber reinforced natural sandwich composites by vacuum-assisted material extrusion process. <https://doi.org/10.13140/RG.2.2.26091.41760>. (ResearchGate: Preprint)
27. Cao D (2023) Strength enhancement by polylactic-acid matrix modification of continuous carbon-fiber-reinforced composites by a material extrusion process. <https://doi.org/10.13140/RG.2.2.12669.64480>. (ResearchGate: Preprint)
28. Cano S, Gonzalez-Gutierrez J, Sapkota J, Spoerk M, Arbeiter F, Schuschnigg S, Holzer C, Kukla C (2019) Additive manufacturing of zirconia parts by fused filament fabrication and solvent debinding: selection of binder formulation. *Add Manuf* 26:117–128. <https://doi.org/10.1016/j.addma.2019.01.001>
29. Orlovska M, Chlup Z, Baca L, Janek M, Kitzmantel M (2020) Fracture and mechanical properties of lightweight alumina ceramics prepared by fused filament fabrication. *J Eur Ceram Soc* 40:4837–4843. <https://doi.org/10.1016/j.jeurceramsoc.2020.02.026>
30. Zetamix (2022) Datasheet Alumina Zetamix Filament (4 July 2023). <https://zetamix.fr/produit/filament-alumine/>
31. Mutsuddy BC, Ford RG (1995) *Ceramic injection moulding*. Chapman & Hall, London
32. Spoerk M, Gonzalez-Gutierrez J, Sapkota J, Schuschnigg S, Holzer C (2018) Effect of the printing bed temperature on the adhesion of parts produced by fused filament fabrication. *Plast Rub Comp* 47(1):17–24. <https://doi.org/10.1080/14658011.2017.1399531>
33. Pekin S, Bukowski J, Zangvil A (1998) A study on weight loss rate controlled binder removal from parts produced by FDC. In: *Proceedings of the Solid Freeform Fabrication Symposium*, Austin, Texas
34. Agarwala MK, van Weeren R, Bandyopadhyay A, Safari A, Danforth SC, Priedeman WR (1996) Filament feed materials for fused deposition processing of ceramics and metals, in: *Proceedings of the Solid Freeform Fabrication Symposium*, Austin, Texas, United States of America
35. Agarwala M, Jamalabad V, Langrana N, Safari A, Whalen P, Danforth S (1996) Structural quality of parts processed by fused deposition. *Rapid Prototyp J* 2:4–19
36. Onagoruwa S, Bose S, Bandyopadhyay A (2001) Fused deposition of ceramics (FDC) and composites. In: *Proceedings of the Solid Freeform Fabrication Symposium*, Austin, Texas, United States of America
37. Kukla C, Cano S, Kaylani D, Schuschnigg S, Holzer C, Gonzalez-Gutierrez J (2019) Debinding behaviour of feedstock for material extrusion additive manufacturing of zirconia. *Powder Metall* 62:196–204. <https://doi.org/10.1080/00325899.2019.1616139>
38. Abel J, Scheithauer U, Janics T, Hampel S, Cano S, Müller-köhn A, Günther A, Kukla C, Moritz T (2019) Fused filament fabrication (FFF) of metal-ceramic components. 1–13. <https://doi.org/10.3791/57693>
39. Rangarajan S, Qi G (2000) Powder processing, rheology, and mechanical properties of feedstock for fused deposition of Si₃N₄ ceramics. *J Am Ceram Soc* 69:1663–1669
40. Li T, Gonzalez-Gutierrez J, Raguz I, Holzer C, Li M, Cheng P, Kitzmantel M, Shi L, Huang L (2020) Material extrusion additively manufactured alumina monolithic structures to improve the efficiency of plasma-catalytic oxidation of toluene. *Addit Manuf* 101700. <https://doi.org/10.1016/j.addma.2020.101700>
41. Nanoe (2020) Zetamix 3D printing filament. <https://zetamix.fr/en/produit/zetamix-alumina-filament/>. Accessed 11 Jan 2023
42. The Virtual Foundry (2023) Ceramic Filaments. <https://shop.thevirtualfoundry.com/collections/ceramic-filaments>. Accessed 11 Jan 2023
43. Smirnov A, Peretyagin P, Bartolomé JF (2019) *J Eur Ceram Soc* 39:3491–3497
44. Bartolomé JF, Smirnov A, Kurland HD, Grabow J, Müller FA (2016) *Sci Reports* 6:20589
45. Smirnov A, Seleznev A, Solis W, Pristinitskiy Y, Peretyagin P, Bartolomé JF (2019) *Nanomaterials* 9(10):1391
46. Smirnov A, Podrabinnik PA, Babushkin NN, Kuznetsova EV, Pristinitskiy YO, Khmyrov RS. Development of Al₂O₃ and PLA ceramic-polymer filament for 3D printing fused deposition modeling method. *AIP Conf Proc* 2467: 020047-1-020047-7. <https://doi.org/10.1063/5.0092881>
47. Auffray L, Gouge PA, Hattali ML (2021) Design of experiment analysis on tensile properties of PLA samples produced by fused filament fabrication. *Int J Adv Manuf Technol*. <https://doi.org/10.1007/s00170-021-08216-7>
48. BS EN ISO 527-2: 2019 Plastics - determination of tensile properties - Part 2: Test conditions for moulding and extrusion plastics. <https://www.iso.org/standard/85822.html>
49. DIN EN ISO 6872: 2019-01 Dentistry - Ceramic materials. <https://www.iso.org/standard/59936.html>
50. Kirstein AF, Woolley RM (1967) Symmetrical bending of thin circular elastic plates on equally spaced point supports. *J Res Natl Bur Stand Sect C* 71:1–10
51. Leriche A, Cambier F, Hampshire S (2017) Sintering of ceramics. *Refer Mod Mater Sci Mat Eng*. <https://doi.org/10.1016/B978-0-12-803581-8.10288-7>
52. Terekhina S, Skorniyakov I, Egorov S, Guillaumat L, Tarasova T, Hattali ML (2020) The effect of build orientation on both flexural quasi-static and fatigue behaviours of filament deposited PA6 polymer. *Int J Fatigue* 140:105825. <https://doi.org/10.1016/j.ijfatigue.2020.105825>
53. Sun Q, Rizvi GM, Bellehumeur CT, Gu P (2008) Effect of processing conditions on the bonding quality of FDM polymer filaments. *Rapid Prototyp J* 14:72–80
54. Bellehumeur C, Li L, Sun Q, Gu P (2004) Modeling of bond formation between polymer filaments in the fused deposition modeling process. *J Manuf Process* 6:170–178
55. Damon J, Dietrich S (2019) Process porosity and mechanical performance of fused filament fabricated 316L stainless steel. *Rapid Prototyp J* 7:1319–27. <https://doi.org/10.1108/RPJ-01-2019-0002>
56. Sadaf M, Bragaglia M, Nanni F (2021) A simple route for additive manufacturing of 316L stainless steel via fused filament fabrication. *J Manuf Process* 67:141–150
57. Tosto C, Bragaglia NF, Recca G, Cicala G (2022) Fused filament fabrication of alumina/polymer filament for obtaining ceramic parts after debinding and sintering processes. *Materials* 15(20):7399. <https://doi.org/10.3390/ma15207399>

58. Nötzel D, Hanemann T (2020) New feedstock system for fused filament fabrication of sintered alumina parts. *Materials* 13:4461
59. Gorjan L, Galusca C, Sami M, Sebastian T, Clemens F (2020) Effect of stearic acid on rheological properties and printability of ethylene vinyl acetate based feedstocks for fused filament fabrication of alumina. *Addit Manuf* 36:101391
60. Qunijat Y, Lartigue C, Brown CA, Hattali L (2017) Multi-scale surface characterization in additive manufacturing using CT advances on mechanics, design engineering and manufacturing. Part of the Lecture Notes in Mechanical Engineering book series (LNME). https://doi.org/10.1007/978-3-319-45781-9_28
61. Iyer S, McIntosh J, Bandyopadhyay A, Langrana N, Safari A, Danforth SC, Clancy RB, Gasdaska C, Whalen PJ (2008) Micro-structural characterization and mechanical properties of Si_3N_4 formed by fused deposition of ceramics. *Int J Appl Ceram Technol* 5:127–137
62. Danzer R, Harrer W, Supancic P, Lube T, Wang ZH, Borger A (2007) The ball on three balls test—strength and failure analysis of different materials. *J Eur Ceram Soc* 27:1481–1485
63. Truxová V, Šafka J, Sobotka J, Macháček J, Ackermann M (2022) Alumina manufactured by fused filament fabrication: a comprehensive study of mechanical properties and porosity. *Polym* 14:991